Journal of Structural Geology 101 (2017) 43–57

Contents lists available at ScienceDirect

Journal of Structural Geology

journal homepage: www.elsevier.com/locate/jsg

Quantifying structural controls on fluid flow: Insights from carbonate-hosted fault damage zones on the Maltese Islands

Vilde Dimmen*, Atle Rotevatn, David C.P. Peacock, Casey W. Nixon, Kari Nærland [1]

Department of Earth Science, University of Bergen, PO Box 7800, 5020 Bergen, Norway

ARTICLE INFO

Article history:
Received 16 March 2017
Received in revised form
29 May 2017
Accepted 31 May 2017
Available online 2 June 2017

Keywords:
Fluid flow
Fault
Fracture
Damage zone
Connectivity
Topology

ABSTRACT

Structural complexity along faults (e.g., relay zones, fault intersections and jogs) exert strong controls on fluid flow, yet few attempts have been made to quantify and visualise such relationships. This paper does that using an outcrop-based study of fracture networks in carbonate rocks in Malta. We investigate the spatial distribution of low-porosity cemented mounds within the fracture networks, and the geometry and topology of the fracture networks are characterised. The mounds are associated with low porosity due to selective cementation along the faults, as well as with peaks in connecting node frequency (a topological proxy for network connectivity), and fracture intensity (a fracture abundance proxy for network complexity). Considering the mounds as a record of palaeo-fluid flow and palaeo-fluid-rock-interaction, this work therefore quantifies and visualises the relationship between structural complexity and fluid flow.

1. Introduction

Faults and fractures may exert strong controls on fluid flow and fluid-rock interaction in the shallow crust, where they can act as conduits, barriers, or a combination of the two (Jolley et al., 2007). On the scale of single faults, important factors that control the flow properties include the type and distribution of damage zone structures, fault core composition, cementation as well as the timing of deformation, fluid flow and diagenesis, and more (Caine et al., 1996; Jolley et al., 2007). At the scale of fault and fracture networks (sensu Peacock et al., 2016), important factors to consider include the locations of fault zone complexity, such as relay zones or fault intersections, as these are particularly prone to act as loci for focused fluid flow (e.g., Gartrell et al., 2004; Fossen and Rotevatn, 2016). Such complex zones can affect the flow of several types of fluids, including magma, hydrocarbons and groundwater, which in turn may further influence a wide variety of processes in the Earth's crust, including earthquakes, volcanism, mineralisation, deformation and sediment remobilisation (e.g., Kerrich, 1986; Curewitz and Karson, 1997; Aydin, 2000; Tavarnelli and Pasqui, 2000; Gartrell et al., 2004; Rowland and Sibson, 2004; Shipton et al., 2004; Yoshida et al., 2008; Verhaert et al., 2009; Micallef et al., 2011; Bense et al., 2013; Rotevatn and Bastesen, 2014; Davidson et al., 2016). The flow of fluids in relation to structural complexity have been a subject for various studies (e.g., Oliver, 1996; Caine and Forster, 1999; Eichhubl et al., 2000; Bense and Van Balen, 2004; Dockrill and Shipton, 2010; Davidson et al., 2016; Ono et al., 2016), all of which appear to underpin a general agreement that there is a strong connection between structural complexity and fluid flow. Despite this general consensus, however, there are currently no studies that attempt to systematically and directly *quantify* and *visualise* the relationship between structural complexity and fluid flow. This paper therefore aims to constrain, quantify and visualise this relationship through field-based investigations.

To do this, we investigate fracture systems in metre-scale fault damage zones in Malta (Fig. 1), where localised cemented mounds (Fig. 2) serve as proxies for palaeo-fluid-rock interaction. The work investigates the relationships between the mounds, and how they relate spatially to variations in the geometries and topologies of the fracture networks, in order to elucidate structural controls on palaeo-fluid flow. The objectives are to (i) determine the porosities of host rocks and of the localised mounds; (ii) to analyse the geometries and topologies of the studied fracture networks; and therefore (iii) to visualise and quantify the spatial distribution of structural complexity; (iv) to investigate the spatial correlation

* Corresponding author.
E-mail address: vilde.dimmen@student.uib.no (V. Dimmen).
[1] Now at: ConocoPhillips, Ekofiskvegen 35, 4056 Tananger, Norway.

http://dx.doi.org/10.1016/j.jsg.2017.05.012

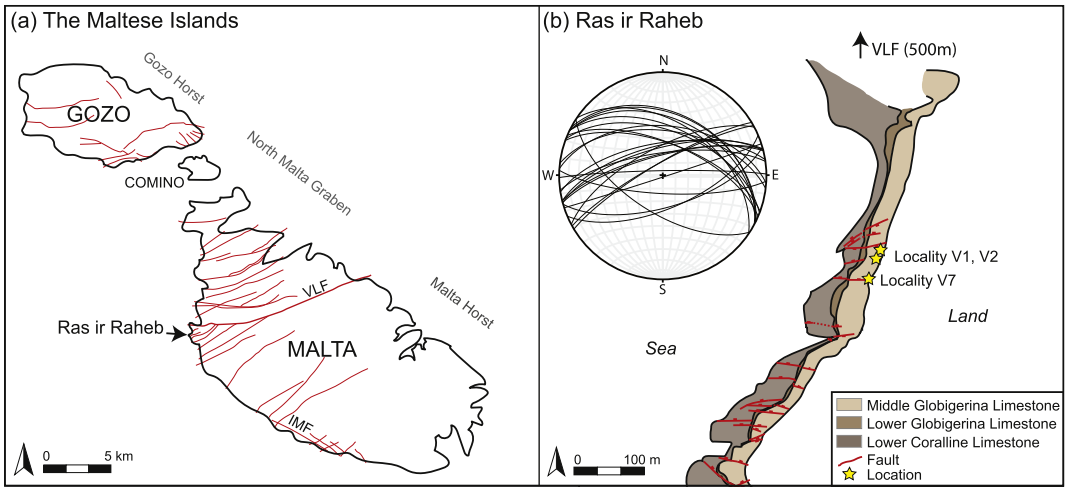

Fig. 1. (**a**) Map of the Maltese Islands (Gozo, Comino and Malta), showing the location of the largest faults in red, and the location of the study area at the western coast of Malta. VLF = Victoria Lines Fault, IMF = Il Maghlaq Fault. After Pedley et al. (1976), Michie et al. (2014), and Missenard et al. (2014). (**b**) Map of the study area at Ras ir Raheb. The stereoplot shows the trends of the normal faults found along the wave-cut platform on which the studied networks are situated. The locations of the fracture networks presented within this paper are marked as locality V1, V2, and V7. After Michie et al. (2014). (For interpretation of the references to colour in this figure legend, the reader is referred to the web version of this article.)

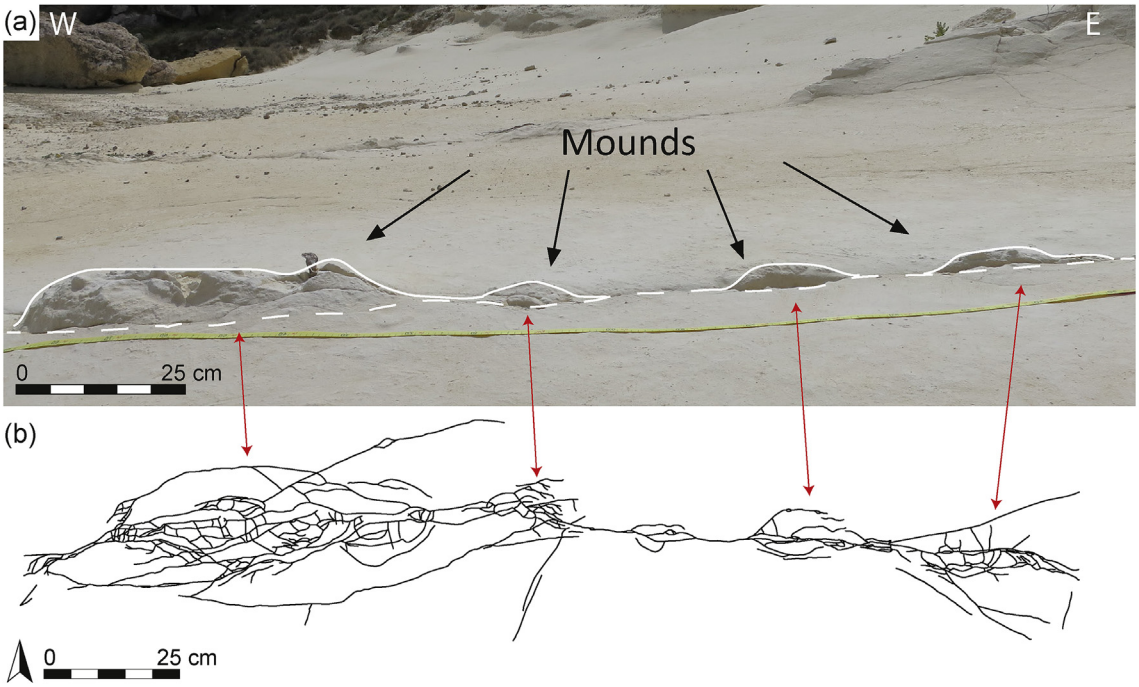

Fig. 2. (**a**) Field photograph of topographic highs, or "mounds", along a fracture network highlighted by the white line. The dashed line indicates ground level/base of the mounds. These mounds were hypothesized to have formed as a result of differential cementation due to localised fluid flow. (**b**) Digitised map of the fracture network depicted in Fig. 2(a). Comparing the digitised map with the photograph of the mounds, we can see how these mounds tend to coincide with the more structurally complex areas of the fracture network.

between cemented mounds and structural complexity within the networks; and, finally, (v) to elucidate structural controls on palaeo-fluid flow and of the interaction between palaeo fluids and host rocks in the studied rocks.

The studied fracture networks are in Miocene-age carbonates of the Globigerina Limestone Formation (Pedley et al., 1976; Dart et al., 1993) located in exceptionally well-exposed outcrops in western Malta (Fig. 1). To quantify and visualise the structural complexity and connectivity of the studied fracture networks, we characterise their *topological properties* (Manzocchi, 2002; Sanderson and Nixon, 2015). Knowledge of the network complexity and connectivity is crucial for the understanding of fluid flow through a rock body, and a topological characterisation offers a more direct route to determine the connectivity and percolation potential of a fracture network than traditional geometric characterisations (Sanderson and Nixon, 2015).

The results of this study have wide-reaching implications, as the ability to quantify and visualise the connection between structural complexity and fluid flow is relevant for a range of geological and economic applications, including for example the generation of

exploration fairway maps for structurally controlled ore mineral deposits, structural seal or retention risk maps in hydrocarbon exploration, and environmental or contaminant risk maps for radon gas, radioactive waste leakage and more.

2. Terminology

We use the term *mound* in this paper to describe mound-shaped, cemented features that stand out with a topographic positive relief along the described fracture networks.

Structurally, we follow the terminology defined by Peacock et al. (2016), with the following additional clarifications.

- We use the term *structurally complex* zones or areas and *structural complexity*, which refer to parts of a fault or fracture network where fracture frequencies are particularly high, and where a wide variation of fracture orientations occurs. Such structurally complex areas typically occur where faults interact, e.g., at relay zones or fault intersections (Tavarnelli and Pasqui, 2000; Fossen et al., 2005; Peacock et al., 2017). Note that here we use *complexity* as a relative term, indicating fractures being more frequent and with a wider range of orientations than other areas, as is typical in fault damage zones.
- The studied fracture networks form parts of the damage zones of small-scale faults (displacements of <1 m), and comprises a combination of joints and faults with cm-scale displacement. The pavement-nature of the outcrops makes it difficult to distinguish between joints and faults due to lack of displacement markers at the cm scale in the relatively homogenous host rocks, and we therefore use the term *fracture* in the descriptions to encompass both joints and faults.

3. Regional tectonic and stratigraphic framework

The Maltese archipelago is on the north-eastern shoulder of the WNW-ESE-trending Pantelleria rift system between Sicily and Tunisia, which formed in the Late Miocene-Early Pliocene due to subduction roll-back associated with the Apennine-Maghrebian subduction zone (e.g., Dart et al., 1993; Jolivet and Faccenna, 2000; Cavazza and Wezel, 2003). The Il Maghlaq Fault (Bonson et al., 2007; Rotevatn et al., 2016), on the southern coast of Malta, is the largest fault (maximum normal displacement of 210 m, Bonson et al., 2007) and is the only tectonic feature on the islands showing the same trend as the Pantelleria Rift system (Fig. 1a) (Illies, 1981; Reuther and Eisbacher, 1985; Gueguen et al., 1998; Micallef et al., 2013). Otherwise, the archipelago is dominated by ENE-WSW trending horst and graben structures, considered to have formed under the same extensional regime as the Pantelleria Rift system (e.g., Dart et al., 1993; Bonson et al., 2007; Putz-Perrier and Sanderson, 2010). The Victoria Lines Fault (VLF), which is the second largest fault on Malta (maximum normal displacement of 90 m), marks the southernmost extent of the North Malta Graben (Fig. 1a) (Pedley et al., 1976). The localities utilised for this study are located 500–1000 m into the footwall of the VLF, at Ras ir Raheb. The studied fracture systems represent damage zones of smaller (displacement less than 1 m) faults, which may be considered as subsidiary faults in the damage zone of the VLF (Fig. 1a).

The stratigraphy of the Maltese islands comprises a shallow marine carbonate succession that can be subdivided into pre-, syn- and post-rift deposits with respect to the Pantelleria rifting event (Fig. 3a; Pedley et al., 1976; Dart et al., 1993; Bonson et al., 2007; Micallef et al., 2013). The pre-rift (> 21 Ma) succession includes the Lower Coralline Limestone Formation platform carbonates and the pelagic carbonates of the Lower Globigerina Limestone Member of the Globigerina Limestone Formation. The syn-rift (21–1.5 Ma) succession consists of the fine-grained foraminiferal and coccolithic Middle (MGLM; the interval of interest in this study) and Upper Globigerina Limestone Members, also of the Globigerina Limestone Formation, followed by the pelagic globigerinid marls and clays of the Blue Clay Formation, the marly glauconite lag of the Greensand Formation, and the Upper Coralline Limestone Formation. A predominantly Quaternary sedimentary succession marks the post-rift depositional sequence, including terrestrial, pelagic and hemipelagic sediments (Pedley et al., 1976; Jongsma et al., 1985; Dart et al., 1993; Micallef et al., 2013).

The MGLM in the study area consists of fine-grained limestones, divided by some thinner layers of phosphoritic conglomerate with an abundance of bivalve-, bryozoan-, solitary coral-, and echinoid-fossils, and is further described in Section 4. The MGLM is here divided into several sub-units (Fig. 3b); the studied fracture networks at Ras ir Raheb are situated within the MGLM-2 unit that consists of a 2–3 m thick interval.

4. Methodology

4.1. Outcrop analyses

A total of six fracture networks were studied in detail (Dimmen, 2016), three of which were selected for full presentation here. The fracture networks represent damage zones of small-scale (displacement <1 m) faults affecting the MGLM. Detailed mapping and structural characterisation of the studied fracture networks were performed in the field. See Section 4.3 for details on fracture network characterisation and quantitative analyses. Additionally, the stratigraphy was recorded by a stratigraphic log of the MGLM at Ras ir Raheb (Fig. 3b). Rock samples were collected from mounds and host rocks (approximately 2 m from the corresponding fracture network) at each locality for petrographic description and porosity analysis (Section 4.2). To record the location of mounds, topographic profiles were collected along the fracture networks, recording the elevation difference relative to a fixed datum (Fig. 4). The fixed datum lines for the topographic profiles were established by stretching a fixed line c. 20–30 cm above the ground, and topography was recorded by measuring the distance from the datum line to the ground.

4.2. Petrographic and porosity analyses

Petrographic- and porosity analysis was undertaken based on thin section analyses using a combination of optical and scanning electron microscopy. Rock samples collected in the field area were saturated with blue epoxy prior to thin section preparation, with the purpose of easier pore space recognition. A Nikon Eclipse 400 POL polarising light microscope was used to analyse the thin sections. A Zeiss Supra 55VP Field Emission Scanning Electron Microscope with a spatial resolution of 0.8 nm and magnification of 500 ×, was used for further analysis of the thin sections. Image-based 2D porosity was determined using the image-processing software ImageJ, following the methods outlined by Røgen et al. (2001). Thin section photomicrographs provide a basis for estimating 2D macroporosity (porosity resolvable using optical microscope imagery), whereas the BSE images allows for a determination of 2D macro- and micro-porosity combined, termed *total porosity* herein. Micro-porosity is porosity that falls below the resolution of optical microscope imagery, but that is resolvable using BSE imagery (Rotevatn et al., 2016). A minimum of 10 photomicrographs were analysed for each thin section; for optical microscopy, half of them were analysed at 4 × magnification, and half at 10 × magnification. For BSE microscopy, a minimum of 10

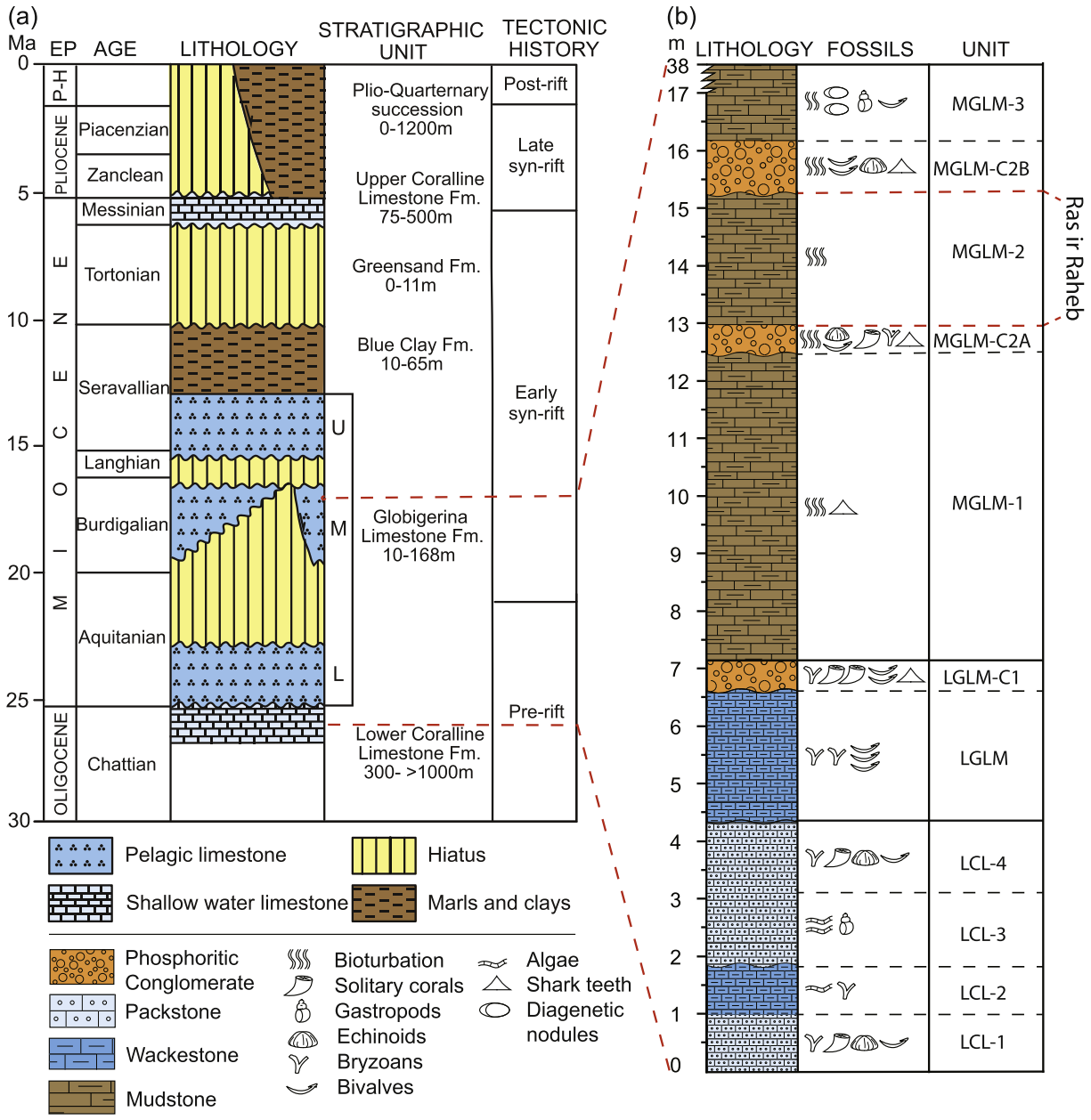

Fig. 3. (**a**) General stratigraphy of the Maltese Islands, showing the pre-, syn-, and post-rift sedimentary succession of Oligocene to Quaternary age. EP = epoch, P-H = Pleistocene-Holocene. From Dart et al. (1993) and Bonson et al. (2007). (**b**) Stratigraphic log from the study area at Ras ir Raheb. LCL = Lower Coralline Limestone, LGLM = Lower Globigerina Limestone Member, MGLM = Middle Globigerina Limestone Member.

images with 500 × magnification were analysed for each thin section.

4.3. Analysis of node and branch topology and its spatial distribution

Fracture data acquisition was undertaken by acquiring high resolution imagery for subsequent detailed analysis in ArcGIS. The studied fracture networks were digitised from the high-resolution outcrop images, and topological characterisation undertaken using an in-house ArcGIS topology toolbox. Topology describes the geometrical relationships of the fractures (e.g., Sanderson and Nixon, 2015), and can be used to characterise the arrangement of fractures within networks and determine their connectivity (Jing and Stephansson, 1997; Manzocchi, 2002; Sanderson and Nixon, 2015). In two dimensions, the topology of a fracture network consists of nodes and branches between nodes (Fig. 5; Manzocchi, 2002; Sanderson and Nixon, 2015). Nodes can be classified into three types depending on their connectivity and geometry: I-nodes represent isolated tips of fractures; Y-nodes are associated with fracture abutments or splays; and X-nodes represent crossing fractures. Y- and X-nodes connect 3 and 4 branches, respectively. Branches have a node at each end which can be an isolated (I-) node or a connecting (Y- or X-) node, thus they can also be classified into three types: isolated I–I branches; singly connected I–C branches; or doubly connected C–C branches (Sanderson and Nixon, 2015).

Sanderson and Nixon (2015) show how the number counts of the different node types (N_I, N_Y, N_X) can be used to calculate further

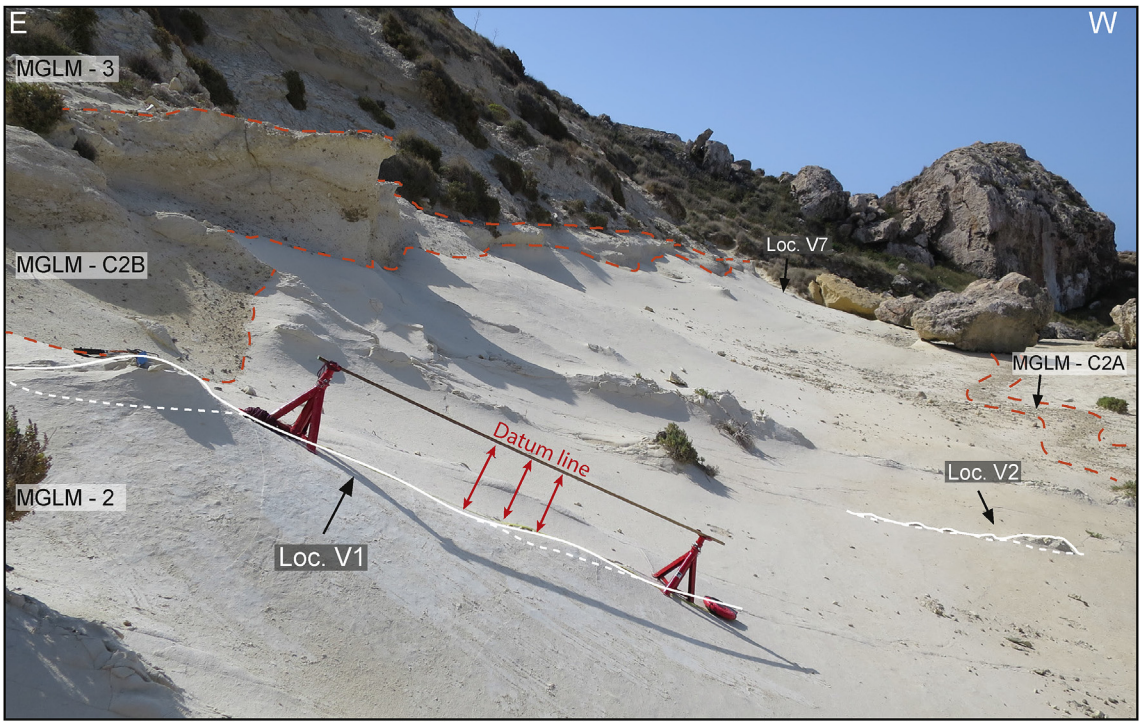

Fig. 4. Overview photograph of the study area, showing the three localities presented in this paper. A fixed datum line above the fracture network of locality V1 in the foreground shows how the topographic profiles were sampled. The distance from the fixed line to the ground was measured in a consistent and systematic manner to record the elevation difference caused by the cemented mounds along the fracture networks. Locality V2 and V7 can be seen in the background.

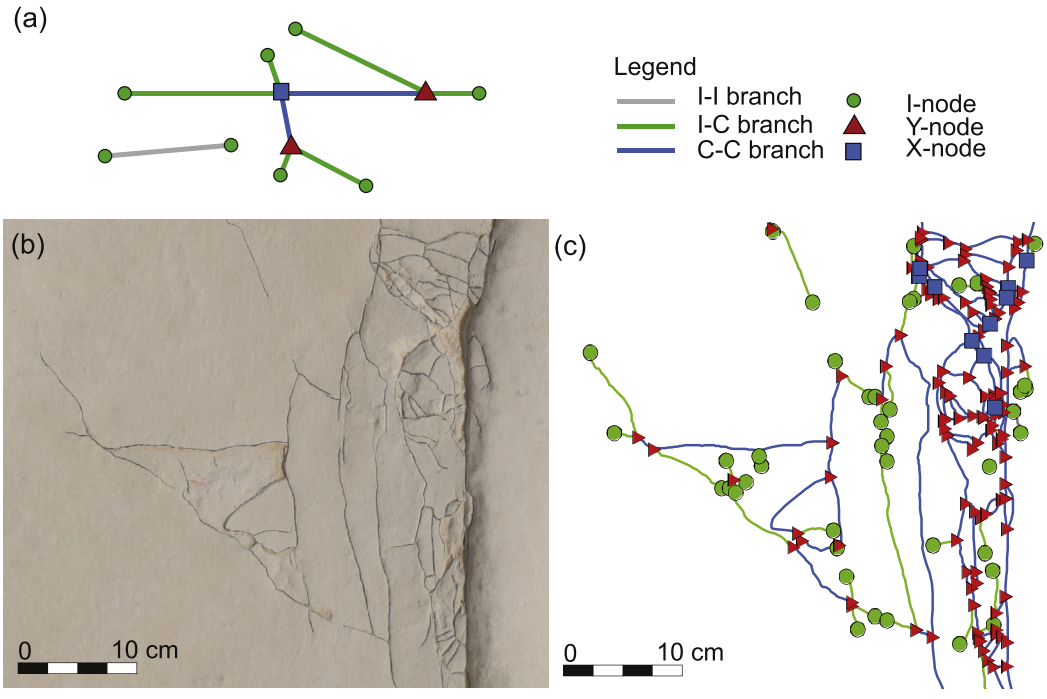

Fig. 5. (**a**) Topological nomenclature, as proposed by Sanderson and Nixon (2015). We differentiate between different types of *nodes* and *branches*. Nodes are isolated nodes (I-nodes), abutting or splaying nodes (Y-nodes), or as crossing nodes (X-nodes). Branches are classified as *isolated* (I–I), *partly connected* (I–C) or *fully connected* (C–C). (**b**) Field photograph showing a part of a fracture network before topological characterisation. (**c**) Digitised fracture network and topological characterisation of the outcrop example shown in (**b**).

topological measures and parameters. These can be used to quantify and describe a network's connectivity, such as the average number of connections per branch (C_B), which describes the degree of connectivity between branches within the network:

$$C_B = (3N_Y + 4N_X) / N_B \quad (1)$$

The number of branches (N_B) is:

$$N_B = (N_I + 3N_Y + 4N_X) / 2 \quad (2)$$

As branches only have two associated nodes, that can be isolated or connected, then values of C_B range from 0 to 2 (for full derivation see Sanderson and Nixon, 2015).

The spatial distribution and variation of different topological parameters and fracture abundances may be visualised to evaluate the distribution of structures and to define *complexity* and connectivity within fracture networks. For this study, we identify the different nodes and branches for each fracture network as a whole, and use the maps to create contour plots of the following parameters: (i) fracture intensities, which presents the total branch length per square metre (m/m^2), illustrating the distribution of branch abundance, and (ii) connecting node frequencies, illustrating variations in the number of connections ($N_C = N_X + N_Y$) per square metre (N_C/m^2).

5. Host rocks

The host rocks of the studied fracture systems comprise parts of the MGLM unit (MGLM-2 in Fig. 3b). The MGLM is comprised of fine-grained limestones, predominantly featuring skeletal fragments, and most abundantly the planktonic foraminifera *Globigerina*. The globigerinids are generally well-preserved, with most of the chambers being intact, contributing to the dominating intragranular porosity of the rock (Fig. 6a). Inter-granular porosity is found between grains, but is less prominent. The grain sizes of the foraminifera are generally in the range of 10–20 μm, but whole foraminifer shells with sizes up to 250 μm occur. Calcite cement is observed on some of the foraminifer shells and in open spaces around the samples (Fig. 6b), interpreted to be dogtooth cement. The cement growth does not seem to favour any type of foraminifera or other features, but appear at various degrees throughout the samples. Some quartz grains with an average size of 120 μm also occur within the samples but are less common (Fig. 6a).

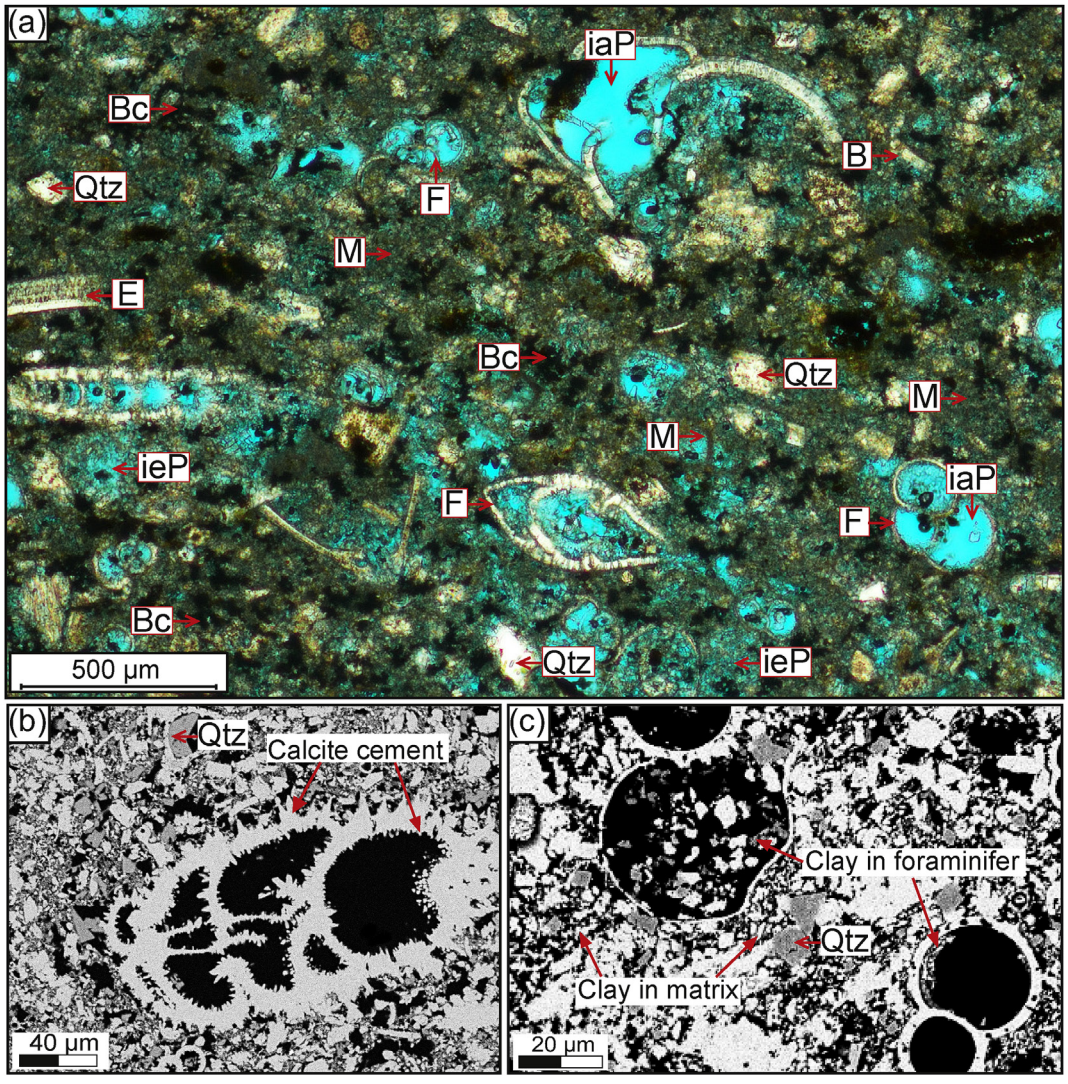

Fig. 6. (**a**) Photomicrograph in plane polarised light of the MGLM-2, host rock between locality V1 and V2. The clear blue colour is caused by the epoxy in which the sample was prepared, indicating pore space. Fossils of echinoderm fragments (E), bivalves (B), and foraminifera (F) are highlighted, as well as the inter- (ieP) and intragranular (iaP) porosity and matrix (M). Dark brown to black patches are thought to be bacterial shrubs (Bc) as a result of hydrothermal activity. Qtz = quartz grains. (**b**) BSE-SEM image, showing calcite cement (dog tooth) growth on both the inside and outside of a foraminifer shell. The black areas represent pore space. (**c**) BSE-SEM image, showing how fine-grained clay material can be observed both in the matrix and inside some of the foraminifer chambers. The foraminifera pointed out here do not show calcite cement growth. (For interpretation of the references to colour in this figure legend, the reader is referred to the web version of this article.)

Fine to cryptocrystalline matrix appears under the optical microscope as a dark brown mass between grains and within foraminifer shells and consist of small ($\leq$ 2 μm) fragments that based on SEM analyses were identified as carbonate fragments, clay minerals and quartz (Fig. 6a and c).

6. Porosity distribution

The digital image analyses of the photomicrographs reveal a subtle but statistically significant difference between the porosity of the host rocks and the localised mounds. The results for 2D macroporosity derived from optical imagery analyses are presented in Fig. 7a, where each data point represents an analysis of one photomicrograph, and each column represents one thin section. The results show great variations within each thin section and each sample. The overall general trend, however, is a slightly higher porosity in the host rock than the corresponding mounds, with a mean porosity of 3.3% for the mounds and 4.1% for the host rocks. This difference is statistically significant, as discussed later in this section.

Fig. 7b shows the total porosity derived from the analysis of BSE-SEM imagery. The analysis of the BSE-SEM images yields overall significantly higher porosity values than the values attained using optical microscopy, showing an average total porosity of 12.2% for the mounds and 14.0% for the host rocks. This is because both macro- and micro-porosity are resolved, in contrast with the optical imagery, where only the macro-porosity is resolved and so lower porosity values are recorded.

The difference in the 2D total porosity between mounds and host rocks can be visually observed when comparing binary BSE-SEM images (Fig. 8). Considering these images from locality V1 as an example, it can be confirmed by visual inspection that it has a higher host rock porosity (measured to 16.5%) compared with the pore space present in the corresponding mound (measured to 10.7%).

Porosity statistics show that the values of the porosity measurements plot linearly ($R = 0.98$ for BSE-SEM images and $R = 0.99$ for photomicrographs) in a cumulative probability scale, indicating that the values are normal graded. They can therefore be used in parametric tests to see if the populations show any significant differences in variance (squared standard deviation) or average values. Snedecor's F-test was used to check if the populations show significant differences in variance, while a Student's t-test was used to check if the average values of the populations show significant

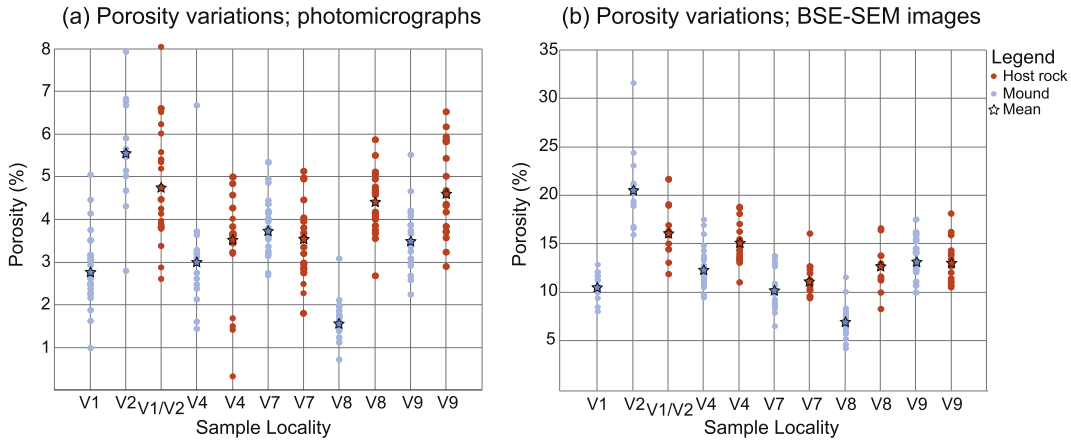

Fig. 7. Data from the thin section samples from mound and host rock at each locality. (**a**) Results from the analysis of microphotographs. (**b**) Results from the analysis of BSE-SEM images. Each dot represents one analysed photograph, and each column represents one thin section. The overall general trend shows a slightly higher porosity in the host rock compared with the mounds.

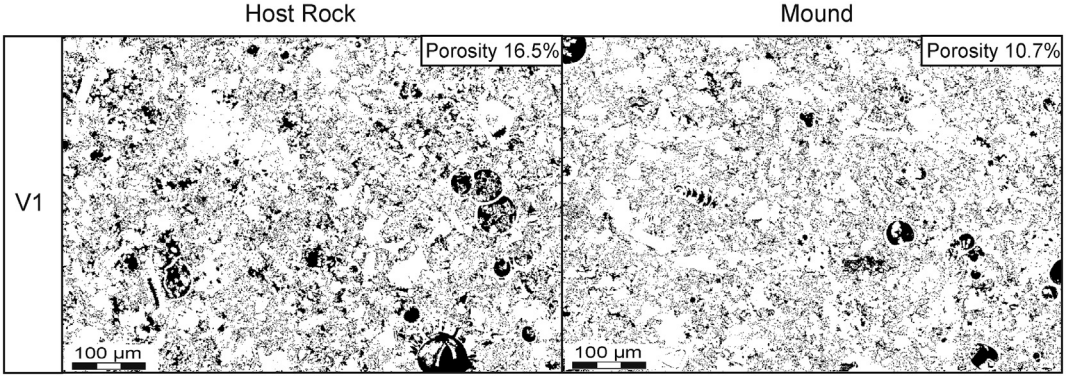

Fig. 8. Comparison of binary BSE-SEM images from the host rock and the corresponding mound for localities V1, V2 and V7. The pore space is displayed in black, and the general porosity for each thin section in which the image is retrieved is pointed out in the uppermost right hand corner of each image (i.e., it is not the porosity for the image displayed here).

differences. The level of significance is described by the factor α; a low α-value indicate a test of high significance.

The results from Snedecor's F-test show that the variance for the mound values are greater than the variance for the host rock values for both the 4 × and 500 × magnification, both with $\alpha = 0.0005$, while the variances are not significantly different for the 10 × magnification dataset, which got $\alpha = 0.005$. The results from the Student's t-test show that average value for the host rock is significantly greater than the average value for the mound for all of the three data sets. The statistical tests confirm that the mounds are associated with an overall lower porosity than the surrounding host rocks, and that the differences are statistically significant. These porosity variations are interpreted to reflect the results of selective and localised cementation of the mounds. Localised cementation does also explain the topographic relief of the mounds, since their increased cementation make them more resistant to weathering than the surrounding host rocks.

7. Geometry and topology of the fracture networks

To investigate the spatial and causal relationship between the cemented mounds and the fracture networks, we present a quantitative geometrical and topological analysis of the networks. A total of six localities with cemented mounds were investigated (Dimmen, 2016), all situated in the MGLM-2 unit immediately south of Ras ir Raheb (Fig. 1b). The mounds generally exhibit an elliptical shape and vary in size with the long axis ranging from 10 to 100 cm; the specific size and shape of each mound is recorded by the topographic profiles presented for each locality. The fracture networks represent damage zones of normal faults with less than 2 m of displacement, and are comprised of smaller faults (displacement generally up to a few centimetres) and joints. All of the studied fracture networks show a varying degree of structural complexity along strike. Out of the six localities, we have selected three for full presentation in the following (Localities V1, V2 and V7, shown in Figs. 9–11, respectively). All of the fracture networks have been studied in pavement outcrops (sub-horizontal to ~20° seaward dipping outcrop surfaces), providing excellent map-view exposure where the along-strike variability of the fracture networks may be studied in detail.

Greatest structural complexity occurs in zones where two fracture segments coalesce to form hard-linked relays, or in intersections where one fracture segment splays or abuts against another. The structurally complex zones are distributed along main fault or fracture traces, extending 10–100 cm along strike, separated by less complex zones. Figs. 9–11 portray: (a) the digitised fracture networks; (b) fracture intensity maps; (c) connecting node frequency maps; (d) graphs showing the fracture intensities; (e) connecting node frequencies; and (f) topographic profiles. The graphs and the topographic profiles for each fault zone were recorded along the same line for each locality, marked in (a) in every figure. The more structurally complex zones at each locality generally coincide with mounds along the fracture network. The topological characterisation shows that these zones generally also coincide with areas of higher connecting node frequencies and fracture intensities.

7.1. Example 1, locality V1

The fracture network of locality V1 covers 3.5 m of a fault zone, and consists of three main segments oriented E-W to NE-SW (Segments I, II and III in Fig. 9a). Five complex zones, marked A-E, are recognised (Fig. 9a). These zones all correspond with areas of higher fracture intensities and higher connecting node frequencies (Fig. 9b and c). The topography profile in (Fig. 9f) shows that the large topographic high at the eastern end of the profile also corresponds with complex zone E (Fig. 9a), and shows an increase in connecting node frequency (Fig. 9e) and fracture intensity (Fig. 9d). The complex zones C and D (Fig. 9a) correspond with peaks in fracture intensities (Fig. 9d) and connecting node frequencies (Fig. 9e). In the topographic profile (Fig. 9f), a wide (c. 80 cm) mound corresponds with the two complex zones C and D combined. Complex zones A and B (Fig. 9a), are associated with peaks in fracture intensity and connecting node frequencies, (Fig. 9d and e), and represent areas of high intensity intensities and connecting node frequencies (Fig. 9b and c). Complex zones A and B are not associated with mounds, as recorded by the topographic profile (Fig. 9f).

7.2. Example 2, locality V2

Locality V2 consists of a 2.75 m long fracture network, oriented E-W (Fig. 10a), which can be divided into two main segments (Segments I and II in Fig. 10a). Segment I consists of one relatively large complex zone, A (Fig. 10a), and connects with segment II through complex zone B (Fig. 10a). Segment II constitutes the eastern half of the system and contains three smaller complex zones, indicated as C, D and E (Fig. 10a).

The complex zones show higher fracture intensities (Fig. 10b) and higher frequencies of connecting nodes (Fig. 10c). The complex zones also coincide with peaks in the graphs of fracture intensity, connecting node frequency, and topography (Fig. 10d–f). The positive correlation is most obvious for the largest mound in complex zone A, for which both the fracture intensity graph (Fig. 10d), the connecting node frequency graph (Fig. 10e), and the topographic profile (Fig. 10f) show positive curves. Complex zone B show positive correlations for both the fracture intensity (Fig. 10d) and the connecting node frequency (Fig. 10e) graphs, but is not as evident in the topographic profile (Fig. 10f). Complex zone C can be recognised through a minor peak in all three graphs (Fig. 10d–f), while complex zones D and E, which is a bit larger than complex zone C, shows a somewhat higher peak in the fracture intensity graph (Fig. 10d) and the connecting node frequency graph (Fig. 10e) than complex zone C.

7.3. Example 3, locality V7

This locality is limited to a 3 m portion of a W-trending normal fault, which shows a throw of 7 cm in an overlying bed of phosphoritic conglomerate. The fracture network is composed of two E-W oriented main segments (Segments I and II in Fig. 11a), linked together in a hard-linked relay zone, and four complex zones marked A-D (Fig. 11a). Segment I comprises the western half of the locality, where complex zone A forms the western part of the relay that links the two segments (Fig. 11a). This breached relay constitutes complex zone B (Fig. 11a), which is the largest complex zone of locality V7. The smaller complex zones C and D are located along segment II, in the eastern part of the locality (Fig. 11a).

The complex zones show higher fracture intensities (Fig. 11b) and higher connecting node frequencies (Fig. 11c). Complex zone B is the highest peak in the topographic profile (Fig. 11f), the fracture intensity graph (Fig. 11d), and the connecting node frequency graph (Fig. 11e). Complex zone A shows a positive correlation with the fracture intensity graph (Fig. 11b) and the connecting node frequency graph (Fig. 11c). A peak in all three graphs (Fig. 11d–f) can be correlated with complex zone C, while complex zone D can be recognised in the graph showing the connecting node frequencies (Fig. 11e), but are not recorded in the fracture intensity graph (Fig. 11d) or the topographic profile (Fig. 11f).

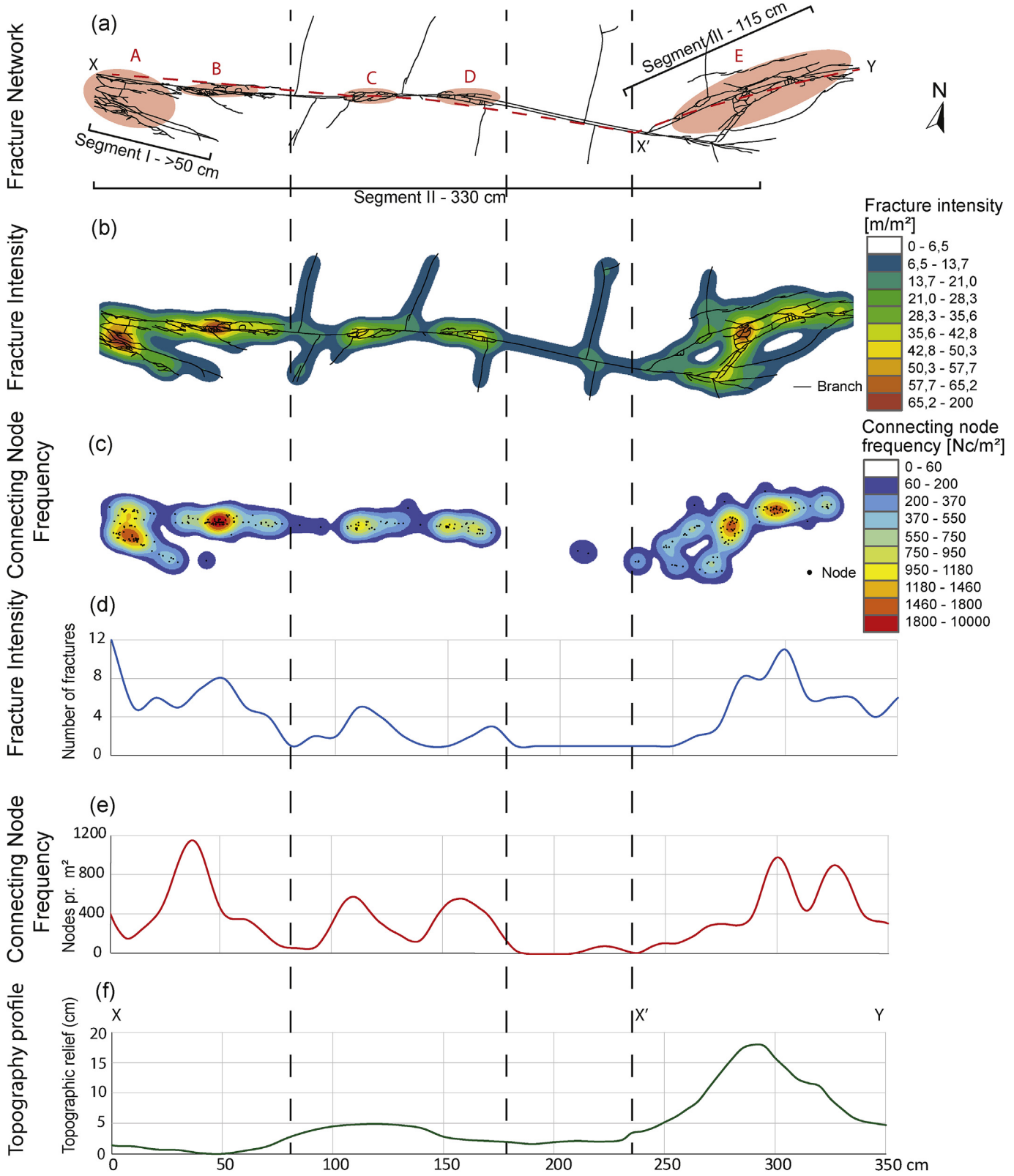

Fig. 9. (**a**) Digitised map of the fracture network at locality V1, showing three main segments. The more structurally complex zones are marked with soft red and labelled A-E. (**b**) Contour map, showing the fracture abundance measure "fracture intensity". (**c**) Contour map showing the topological parameter "connecting node frequency". (**d**) Graph collected along the red dashed line in Fig. 9(a), showing the fracture intensity-. (**e**) Graph collected along the red dashed line in Fig. 9(a), showing the connecting node frequency along the network. (**f**) Topographic profile, collected along the red, dashed line in Fig. 9(a), showing the relief variations along the fracture network. The dashed black lines are guides for easier correlation between the maps and graphs. (For interpretation of the references to colour in this figure legend, the reader is referred to the web version of this article.)

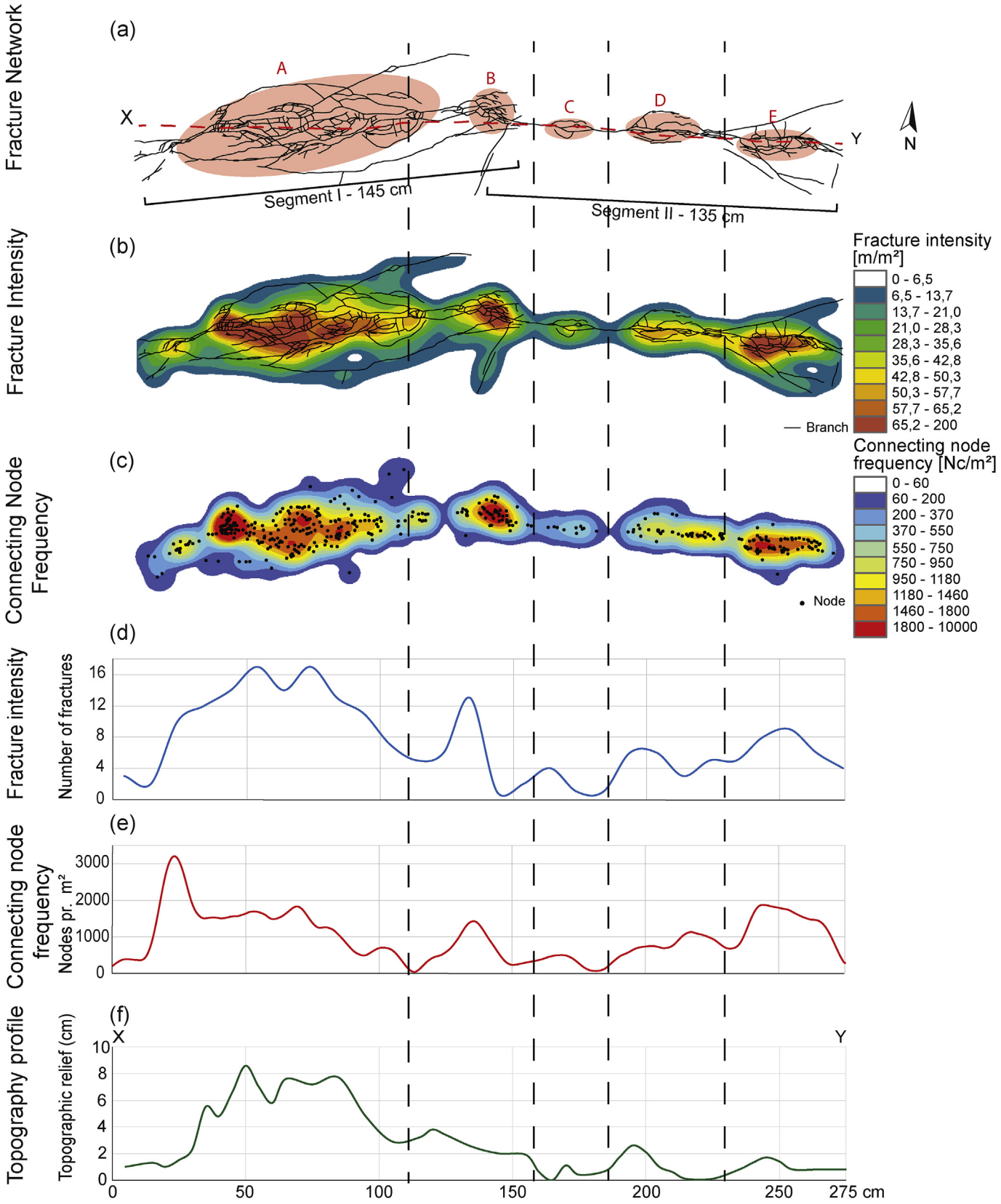

Fig. 10. (**a**) Digitised map of the fracture network at locality V2, showing three main segments. The more structurally complex zones are marked with soft red and labelled A-E. (**b**) Contour map, showing the fracture abundance measure "fracture intensity". (**c**) Contour map showing the topological parameter "connecting node frequency". (**d**) Graph collected along the red dashed line in Fig. 10(a), showing the fracture intensity. (**e**) Graph collected along the red dashed line in Fig. 10(a), showing the connecting node frequency along the network. (**f**) Topographic profile, collected along the red, dashed line in Fig. 10(a), showing the relief variations along the fracture network. The dashed black lines are guides for easier correlation between the maps and graphs. (For interpretation of the references to colour in this figure legend, the reader is referred to the web version of this article.)

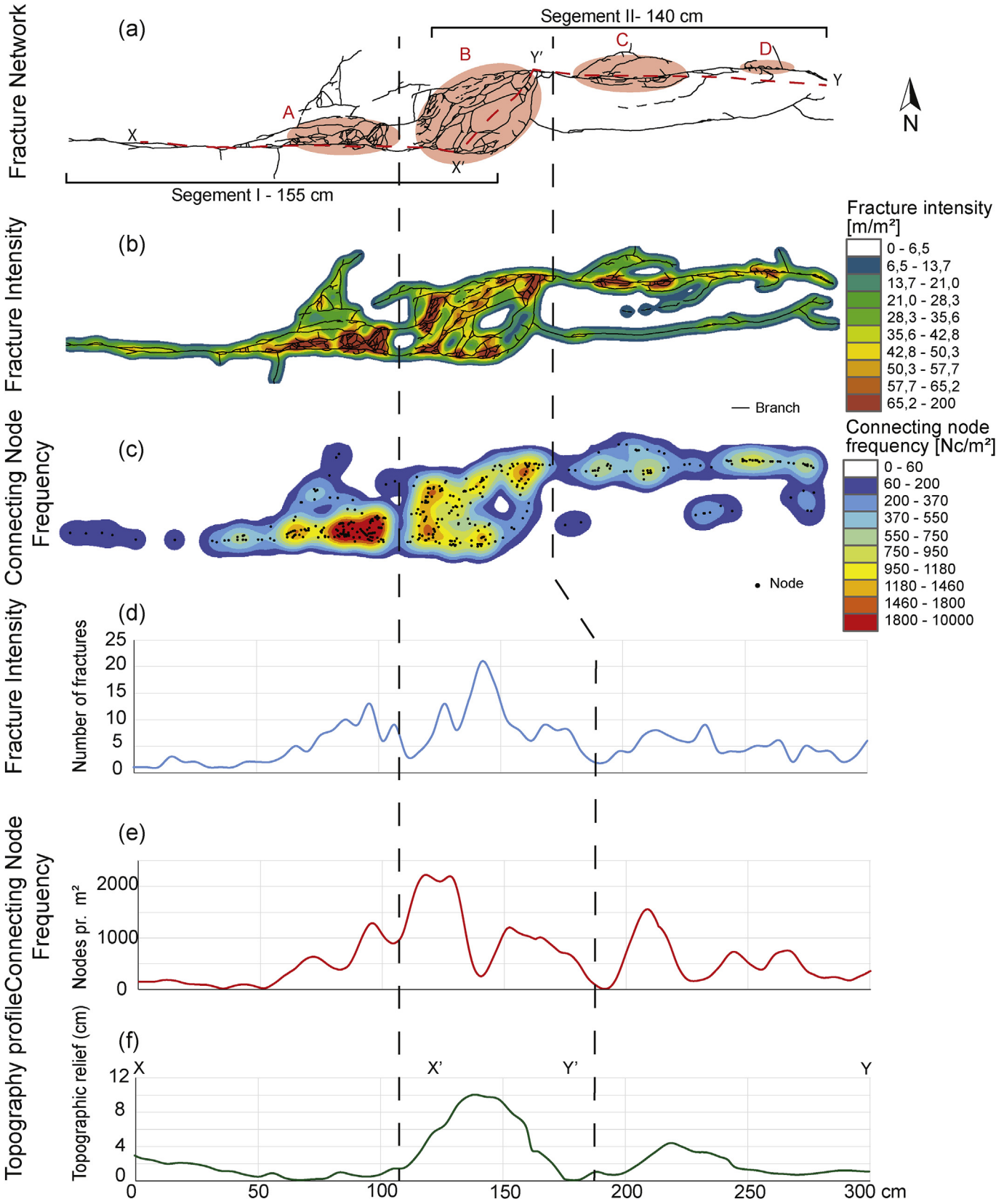

Fig. 11. (**a**) Digitised map of the fracture network at locality V7, showing three main segments. The more structurally complex zones are marked with soft red and labelled A-D. (**b**) Contour map, showing the fracture abundance measure "fracture intensity". (**c**) Contour map showing the topological parameter "connecting node frequency". (**d**) Graph collected along the red dashed line in Fig. 11(a), showing the fracture intensity. (**e**) Graph collected along the red dashed line in Fig. 11(a), showing the connecting node frequency along the network. (**f**) Topographic profile, collected along the red, dashed line in Fig. 11(a), showing the relief variations along the fracture network. The dashed black lines are guides for easier correlation between the maps and graphs. (For interpretation of the references to colour in this figure legend, the reader is referred to the web version of this article.)

8. Discussion

The porosity analyses presented in Section 6 show that the mounds are associated with lower porosity compared with the surrounding host rocks. Based on this, we attribute the formation of the mounds to localised increases in palaeo-fluid-rock-interaction in the form of selective cementation, which led to the mounds being resistant to weathering and therefore forming topographic highs on the outcrops. In the following, we discuss the spatial distribution of the mounds relative to variability of the geometric and topological properties of the fracture network presented in Section 7, to elucidate the relationship between network complexity and past fluid-rock interaction.

The studied fracture networks show that the low-porosity mounds are preferentially developed in the parts of the fracture networks that are associated with high fracture intensities and connecting node frequencies (Figs. 9–11). High fracture intensity indicates that the network is structurally complex, while high connecting node frequency indicates that the fractures in the network are well connected, and that the network itself is highly connected (cf. Morley and Nixon, 2016). The trend is therefore that the complex and well-connected parts of the fracture networks coincide with evidence for palaeo-fluid-flow in the form of cemented mounds. Having established this spatial correlation, two key questions that arise are "how do the structurally complex zones form?" (Section 8.1), and "what is their role in controlling the localisation of flow?" (Section 8.2).

8.1. How do structurally complex zones form?

Faults and other types of fractures generally form zones that consist of several segments that interact, i.e., jog, bifurcate and/or link, creating networks of longer, continuous faults or other types of fractures with irregularities like fault bends and fault intersections (e.g., Peacock and Sanderson, 1991, 1994; Cartwright et al., 1995; Mansfield and Cartwright, 1996; Tavarnelli and Pasqui, 2000; Walsh et al., 2003; Rotevatn and Bastesen, 2014; Peacock et al., 2017). Such irregularities may cause greater stress and local stress concentrations, which further induce small-scale fracturing along and around the fault plane, resulting in zones of higher complexity (Segall and Pollard, 1980; Maerten et al., 2002). Perturbation of the stress field around faults during their growth affects the development of joints in proximity to the fault, tending to make fractures grow at high angles to the faults (Tamagawa and Pollard, 2008). Interaction of the local stress fields around overlapping fault tips leads to a locally increased shear stress (Crider and Pollard, 1998) and rotation of the stress field as a function of the σ_1/σ_2 principal stress ratio (Kattenhorn et al., 2000). Therefore, high fracture intensities and variable fracture orientations are to be expected. As the zones of structural complexity associated with the studied fracture networks are all found in conjunction with relay zones or intersections between the main fracture segments of the networks, we interpret that the areas of structural complexity formed due to fracture interaction, stress enhancement and stress perturbation during fault growth.

8.2. What is the role of structural complexity for controlling flow?

Structurally complex zones are areas of elevated fracture abundance and complexity, which tend to act as fluid flow conduits (e.g., Berkowitz, 1995; Gartrell et al., 2004). Fluids tend to localise and flow in and along the abundant fractures (if open) in the structurally complex zones (Davatzes and Aydin, 2003) (Fig. 12). Two types of fluid flow conduits along active faults can be identified. One type are conduits along the fault plane caused by dilation associated with slip, and the second type are created by secondary structures near fault tips and other structurally complex zones such as relays and fault intersections (Martel, 1990; Barton et al., 1995; Martel and Boger, 1998; Kattenhorn et al., 2000; Davatzes and Aydin, 2003; Tamagawa and Pollard, 2008). These secondary structures are an especially important pathway for fluid flow in tight carbonate rocks with low matrix permeability (Tamagawa and Pollard, 2008; Casini et al., 2011; Rotevatn and Bastesen, 2014).

The complex zones documented at the localities in this study show high fracture intensities and high degrees of network connectivity recorded by high connecting node frequencies. In the following, we discuss the physical mechanisms that explain why structurally complex zones can represent conduits for localised flow. One reason is that open fractures are associated with high permeability in contrast to a low-porous host rock, and a structurally complex zone with high fracture intensity, various fracture orientations and high connectivity would represent a particularly high-permeable fluid conduit (e.g., Rotevatn and Bastesen, 2014). Secondly, stress perturbation may also provide wider fracture apertures to further increase permeability in areas of fault interaction, relay zones or fault tips (Tamagawa and Pollard, 2008). Thirdly, the great variety of fracture orientations in such areas mean that for any given stress field, there is a great chance that some of the fractures are optimally oriented to be kept open (Sanderson and Zhang, 2004).

8.3. The relative roles of increased flow vs. increased fluid-rock reactions

The mounds along the studied fracture networks show a lower porosity than the host rock, which we interpret to be a result of increased fluid flow because the mounds coincide with structurally complex zones. Increased fluid flow could cause more cementation, as more mineralising fluids can pass through the rock (e.g., Flügel, 2010). The mounds may not only be a record of increased flow, however, and other mechanisms may operate. For example, the increased cementation may be a result of increased fluid-rock reactions in the complex areas, caused by intense fracturing. The increased number of fractures in the complex zones fragment the rock volume, leading to a larger reactive surface area available to the mineralising fluids (Lüttge et al., 1999; Flügel, 2010). We suggest that, in the structurally complex zones in this study area, a combination of (i) increased fluid flow and (ii) high reactive surface area caused increased fluid-rock interaction and, therefore, localised cementation and mound formation.

8.4. Implications of being able to understand and quantify structural controls on fluid flow

As shown here, structural complexity may control localised flow and fluid-rock reactions, and structural complexity may be quantified by characterising the geometric and topological properties of fault and fracture networks. In the following, we elaborate on the implications of understanding structural controls on flow, and the applications of being able to quantify structural complexity.

Understanding structural complexity and its controls on fluid flow has a wide range of implications and applications. For example, Davidson et al. (2016) examine radon (^{222}Rn) anomalies due to upward migration of fluids along fault zones in New Zealand. They show that the concentration of radon isotopes is generally higher near faults and fault intersections, indicating a positive correlation between structural complexity and the flow of radon gas. Similar results have been reported from India (Virk and Singh, 1993), California (King et al., 1996), Egypt (Moussa and El Arabi, 2003), and Japan (Igarashi et al., 1995). Rowland and Sibson

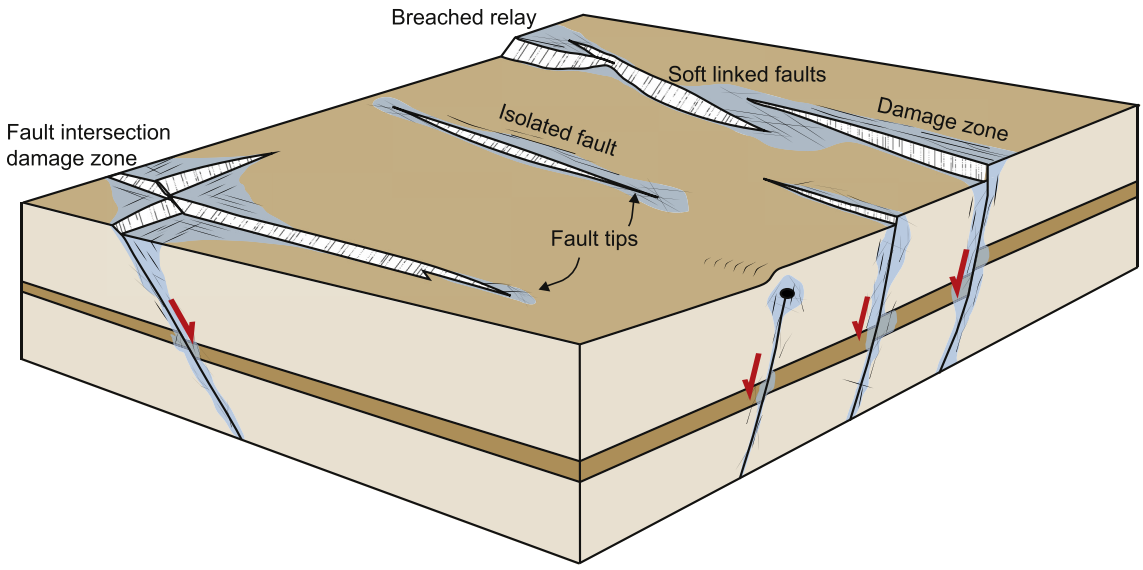

Fig. 12. Schematic illustration of preferential fluid localisation, illustrated by the blue colour, along faults and fault intersections (after Peacock et al., 2016). Fluid flow may localise in fault damage zones and along fault planes, especially in more complex zones, such as linkage points, fault tips and fault intersections. (For interpretation of the references to colour in this figure legend, the reader is referred to the web version of this article.)

(2004) and Curewitz and Karson (1997) identify relationships between structural complexity and hydrothermal activity, and show that concentrations of geothermal zones and the positions of hot springs coincide with increased vertical flow at fault steps, relays and fault intersections. Gartrell et al. (2004) examine the effect of fault intersections on hydrocarbon seal breach through three-dimensional numerical modelling, and show that zones of high dilation are generated close to fault intersections, leading to high permeable zones with a concentration of open fractures ideal for fluid migration, and therefore escape of hydrocarbons. Fluid flow associated with fault intersections may also affect earthquake rupture, as changes in increase fluid pressure may promote fault slip (Sibson, 1996; Talwani, 1999; Kim et al., 2004). Faults, fractures, and structurally complex zones in the shallow crust can also impact environmental issues, such as CO_2 storage, leakage from radioactive waste disposal sites, contaminant transport, and flow patterns of groundwater (Yoshida et al., 2008; Dockrill and Shipton, 2010; Bense et al., 2013).

The above examples highlight the importance of understanding structural controls on fluid flow for a range of purposes. The techniques used in this study, where we correlate proxies for palaeo-fluid-flow with quantified structural complexity and connectivity, may improve how structural controls on flow are analysed and assessed. For example, being able to quantify and visualise the distribution and magnitude of structural complexity and fault/fracture network connectivity may find applications in the generation of hazard maps for radon gas, earthquake prediction, hydrocarbon seal risk assessment, ore mineral deposits exploration and more.

9. Conclusions

The aims of this paper have been to improve the understanding of structurally controlled fluid flow, and, specifically, to demonstrate a novel approach to quantify and visualise the relationships between fluid flow and structural complexity. Field-based investigation, characterisation of the geometry and topology of fracture networks, and porosity analysis have been used to investigate the relationship between structural complexity and proxies (cemented mounds) for palaeo-fluid flow around small-scale normal faults in carbonate rocks, Malta. The following conclusions are made:

- Mounds exhibit an overall lower porosity (0.3–6% difference) than the host rock, as a result of selective, localised cementation.
- Topological analyses of the fracture networks indicate that areas of fracture interaction (relays, fault intersections), which we term *structurally complex areas*, are associated with higher connecting node frequency and fracture intensities than elsewhere, which indicates that these parts of the fracture networks are highly connected.
- The low-porosity cemented mounds spatially coincide with the structurally most complex and well-connected parts of the fracture networks, indicating that the complex areas are associated with increased fluid-rock interaction.
- Increased fluid-rock interaction in the structurally complex areas are attributed to a combination of two effects. Firstly, the structurally complex areas represent conduits for localised flow of mineralising fluids, due to higher fracture abundancy and high fracture connectivity. Secondly, the intense fracturing in the structurally complex areas lead to greater reactive surface area, promoting an increase in fluid-rock reactions.

The findings have great implications for understanding the relationship between structural complexity and fluid flow, and the quantification and visualisation of structural complexity. Quantification of the relationship between structural complexity and flow has the potential to bring about improvements in the prediction of fluid flow properties in the subsurface. For example, topological characterisation of seismic-scale fault networks based on subsurface data, combined with similar data from analogue studies, may offer a more direct route to quantify and predict subsurface flow properties.

Acknowledgements

We thank Enrico Tavarnelli and an anonymous reviewer for their constructive and positive reviews, leading to improvement and clarification of this paper, and editor Cees Passchier for editorial

guidance. Ray Leadbitter at the Independent Petrographic Services Ltd. in Aberdeen, UK, are thanked for preparation of excellent thin sections. Thanks are given to Gunnar Sælen for helpful discussions concerning the host rock characterisation and for carrying out the geostatistical analysis. Irina Korneva and Toms Buls contributed with advice regarding *ImageJ* and the porosity estimations. Thomas B. Kristensen, Ulrike Freitag and Arild Andresen are thanked for great company and inspiring discussions during fieldwork in Malta, while Carmelo Agius and his wife Anna Aguis, are thanked for hosting us all. BKK is thanked for fundings through the BKK-UiB agreement. Nixon and Dimmen are also supported by scholarships from VISTA, a collaborative program for fundamental research by the Norwegian Academy of Science and Letters, and Statoil. Rotevatn, Peacock, and Nixon further acknowledge support for the ANIGMA project from the Research Council of Norway (project no. 244129/E20) through the ENERGIX program, and Statoil through the Akademia agreement. We thank the University of Bergen for partial funding for publishing this paper open access.

References

Aydin, A., 2000. Fractures, faults, and hydrocarbon entrapment, migration and flow. Mar. Petrol. Geol. 17, 797–814.
Barton, C.A., Zoback, M.D., Moos, D., 1995. Fluid flow along potentially active faults in crystalline rock. Geology 23, 683–686.
Bense, V.F., Gleeson, T., Loveless, S.E., Bour, O., Scibek, J., 2013. Fault zone hydrogeology. Earth-Sci. Rev. 127, 171–192.
Bense, V.F., Van Balen, R., 2004. The effect of fault relay and clay smearing on groundwater flow patterns in the Lower Rhine Embayment. Basin Res. 16, 397–411.
Berkowitz, B., 1995. Analysis of fracture network connectivity using percolation theory. Math. Geol. 27, 467–483.
Bonson, C.G., Childs, C., Walsh, J.J., Schöpfer, M.P.J., Carboni, V., 2007. Geometric and kinematic controls on the internal structure of a large normal fault in massive limestones: the Maghlaq Fault, Malta. J. Struct. Geol. 29, 336–354.
Caine, J.S., Evans, J.P., Forster, C.B., 1996. Fault zone architecture and permeability structure. Geology 24, 1025–1028.
Caine, J.S., Forster, C.B., 1999. Fault zone architecture and fluid flow: insights from field data and numerical modeling. Geophys. Monogr. 113, 101–127.
Cartwright, J.A., Trudgill, B.D., Mansfield, C.S., 1995. Fault growth by segment linkage: an explanation for scatter in maximum displacement and trace length data from the Canyonlands Grabens of SE Utah. J. Struct. Geol. 17, 1319–1326.
Casini, G., Gillespie, P., Vergés, J., Romaire, I., Fernández, N., Casciello, E., Saura, E., Mehl, C., Homke, S., Embry, J.-C., 2011. Sub-seismic fractures in foreland fold and thrust belts: insight from the Lurestan Province, Zagros Mountains, Iran. Pet. Geosci. 17, 263–282.
Cavazza, W., Wezel, F.C., 2003. The Mediterranean region-a geological primer. Episodes 26, 160–168.
Crider, J.G., Pollard, D.D., 1998. Fault linkage: three-dimensional mechanical interaction between echelon normal faults. J. Geophys. Res. Solid Earth 103, 24373–24391.
Curewitz, D., Karson, J.A., 1997. Structural settings of hydrothermal outflow: fracture permeability maintained by fault propagation and interaction. J. Volcanol. Geotherm. Res. 79, 149–168.
Dart, C., Bosence, D., McClay, K., 1993. Stratigraphy and structure of the Maltese graben system. J. Geol. Soc. Lond. 150, 1153–1166.
Davatzes, N.C., Aydin, A., 2003. Overprinting faulting mechanisms in high porosity sandstones of SE Utah. J. Struct. Geol. 25, 1795–1813.
Davidson, J.R.J., Fairley, J., Nicol, A., Gravley, D., Ring, U., 2016. The origin of radon anomalies along normal faults in an active rift and geothermal area. Geosphere 12, 1656–1669.
Dimmen, V., 2016. Structural controls on fluid flow in carbonate rocks: quantitative insights from the Maltese Islands. MSc. thesis. Department of Earth Science. University of Bergen, p. 88. unpublished.
Dockrill, B., Shipton, Z.K., 2010. Structural controls on leakage from a natural CO 2 geologic storage site: central Utah, USA. J. Struct. Geol. 32, 1768–1782.
Eichhubl, P., Greene, H., Naehr, T., Maher, N., 2000. Structural control of fluid flow: offshore fluid seepage in the Santa Barbara Basin, California. J. Geochem. Explor. 69, 545–549.
Flügel, E., 2010. Microfacies of Carbonate Rocks, Analysis, Interpretation and Application, second ed. Springer, Heidelberg.
Fossen, H., Johansen, T.E.S., Hesthammer, J., Rotevatn, A., 2005. Fault interaction in porous sandstone and implications for reservoir management; examples from southern Utah. AAPG Bull. 89, 1593–1606.
Fossen, H., Rotevatn, A., 2016. Fault linkage and relay structures in extensional settings - a review. Earth-Sci. Rev. 154, 14–28.
Gartrell, A., Zhang, Y., Lisk, M., Dewhurst, D., 2004. Fault intersections as critical hydrocarbon leakage zones: integrated field study and numerical modelling of an example from the Timor Sea, Australia. Mar. Petrol. Geol. 21, 1165–1179.
Gueguen, E., Doglioni, C., Fernandez, M., 1998. On the post-25 Ma geodynamic evolution of the western Mediterranean. Tectonophysics 298, 259–269.
Igarashi, G., Saeki, S., Takahata, N., Sumikawa, K., 1995. Ground-water radon anomaly before the Kobe earthquake in Japan. Science 269, 60–61.
Illies, J.H., 1981. Graben formation — the Maltese Islands — a case history. Tectonophysics 73, 151–168.
Jing, L., Stephansson, O., 1997. Network topology and homogenization of fractured rocks. In: Jamtveit, B., Yardley, B.W.D. (Eds.), Fluid Flow and Transport in Rocks. Springer, pp. 191–202.
Jolivet, L., Faccenna, C., 2000. Mediterranean extension and the Africa-Eurasia collision. Tectonics 19, 1095–1106.
Jolley, S.J., Barr, D., Walsh, J., Knipe, R., 2007. Structurally complex reservoirs: an introduction. In: Jolley, S.J., Barr, D., Walsh, J., Knipe, R. (Eds.), Structurally Complex Reservoirs. Geological Society, London, pp. 1–24. Special Publications.
Jongsma, D., van Hinte, J.E., Woodside, J.M., 1985. Geologic structure and neotectonics of the North African continental margin south of Sicily. Mar. Petrol. Geol. 2, 156–179.
Kattenhorn, S.A., Aydin, A., Pollard, D.D., 2000. Joints at high angles to normal fault strike: an explanation using 3-D numerical models of fault-perturbed stress fields. J. Struct. Geol. 22, 1–23.
Kerrich, R., 1986. Fluid infiltration into fault zones: chemical, isotopic, and mechanical effects. Pure Appl. Geophys. 124, 225–268.
Kim, Y.-S., Peacock, D.C.P., Sanderson, D.J., 2004. Fault damage zones. J. Struct. Geol. 26, 503–517.
King, C.-Y., King, B.-S., Evans, W.C., Zhang, W., 1996. Spatial radon anomalies on active faults in California. Appl. Geochem. 11, 497–510.
Lüttge, A., Bolton, E.W., Lasaga, A.C., 1999. An interferometric study of the dissolution kinetics of anorthite: the role of reactive surface area. Am. J. Sci. 299, 652–678.
Maerten, L., Gillespie, P., Pollard, D.D., 2002. Effects of local stress perturbation on secondary fault development. J. Struct. Geol. 24, 145–153.
Mansfield, C.S., Cartwright, J.A., 1996. High resolution fault displacement mapping from three-dimensional seismic data: evidence for dip linkage during fault growth. J. Struct. Geol. 18, 249–263.
Manzocchi, T., 2002. The connectivity of two-dimensional networks of spatially correlated fractures. Water Resour. Res. 38, 1–20.
Martel, S.J., 1990. Formation of compound strike-slip fault zones, Mount Abbot quadrangle, California. J. Struct. Geol. 12, 869–882.
Martel, S.J., Boger, W.A., 1998. Geometry and mechanics of secondary fracturing around small three-dimensional faults in granitic rock. J. Geophys. Res. Solid Earth 103, 21299–21314.
Micallef, A., Berndt, C., Debono, G., 2011. Fluid flow systems of the Malta plateau, central Mediterranean Sea. Mar. Geol. 284, 74–85.
Micallef, A., Foglini, F., Le Bas, T., Angeletti, L., Maselli, V., Pasuto, A., Taviani, M., 2013. The submerged paleolandscape of the Maltese Islands: morphology, evolution and relation to Quaternary environmental change. Mar. Geol. 335, 129–147.
Michie, E., Haines, T., Healy, D., Neilson, J., Timms, N.E., Wibberley, C., 2014. Influence of carbonate facies on fault zone architecture. J. Struct. Geol. 65, 82–99.
Missenard, Y., Bertrand, A., Vergély, P., Benedicto, A., Cushing, M.-E., Rocher, M., 2014. Fracture-fluid relationships: implications for the sealing capacity of clay layers - insights from field study of the Blue Clay formation, Maltese islands. Bull. Soc. Géol. Fr. 185, 51–63.
Morley, C., Nixon, C., 2016. Topological characteristics of simple and complex normal fault networks. J. Struct. Geol. 84, 68–84.
Moussa, M.M., El Arabi, A.-G.M., 2003. Soil radon survey for tracing active fault: a case study along Qena-Safaga road, Eastern Desert, Egypt. Radiat. Meas. 37, 211–216.
Oliver, N., 1996. Review and classification of structural controls on fluid flow during regional metamorphism. J. Metamorph. Geol. 14, 477–492.
Ono, T., Yoshida, H., Metcalfe, R., 2016. Use of fracture filling mineral assemblages for characterizing water-rock interactions during exhumation of an accretionary complex: an example from the Shimanto Belt, southern Kyushu Japan. J. Struct. Geol. 87, 81–94.
Peacock, D.C.P., Nixon, C., Rotevatn, A., Sanderson, D., Zuluaga, L., 2016. Glossary of fault and other fracture networks. J. Struct. Geol. 92, 12–29.
Peacock, D.C.P., Nixon, C.W., Rotevatn, A., Sanderson, D.J., Zuluaga, L.F., 2017. Interacting faults. J. Struct. Geol. 97, 1–22.
Peacock, D.C.P., Sanderson, D.J., 1991. Displacements, segment linkage and relay ramps in normal fault zones. J. Struct. Geol. 13, 721–733.
Peacock, D.C.P., Sanderson, D.J., 1994. Geometry and development of relay ramps in normal fault systems. AAPG Bull. 78, 147–165.
Pedley, H., House, M., Waugh, B., 1976. The geology of Malta and Gozo. Proc. Geolo. Assoc. 87, 325–341.
Putz-Perrier, M.W., Sanderson, D.J., 2010. Distribution of faults and extensional strain in fractured carbonates of the North Malta Graben. Am. Assoc. Petrol. Geol. Bull. 94, 435–456.
Reuther, C.-D., Eisbacher, G., 1985. Pantelleria Rift - crustal extension in a convergent intraplate setting. Geol. Rundsch. 74, 585–597.
Rotevatn, A., Bastesen, E., 2014. Fault linkage and damage zone architecture in tight carbonate rocks in the Suez Rift (Egypt): implications for permeability structure along segmented normal faults. In: Spence, G.H., Redfern, J., Aguilera, R., Bevan, T.G., Cosgrove, J.W., Couples, G.D., Daniel, J.-M. (Eds.), Advances in the Study of Fractured Reservoirs. Geological Society, London, pp. 79–95. Special

Publications.
Rotevatn, A., Thorsheim, E., Bastesen, E., Fossmark, H.S.S., Torabi, A., Sælen, G., 2016. Sequential growth of deformation bands in carbonate grainstones in the hangingwall of an active growth fault: implications for deformation mechanisms in different tectonic regimes. J. Struct. Geol. 90, 27–47.
Rowland, J., Sibson, R., 2004. Structural controls on hydrothermal flow in a segmented rift system, Taupo Volcanic Zone, New Zealand. Geofluids 4, 259–283.
Røgen, B., Gommesen, L., Fabricius, I.L., 2001. Grain size distributions of chalk from image analysis of electron micrographs. Comput. Geosci. 27, 1071–1080.
Sanderson, D.J., Nixon, C.W., 2015. The use of topology in fracture network characterization. J. Struct. Geol. 72, 55–66.
Sanderson, D.J., Zhang, X., 2004. Stress-Controlled Localization of Deformation and Fluid Flow in Fractured Rocks. Geological Society, London, Special Publications 231, pp. 299–314 unpublished.
Segall, P., Pollard, D.D., 1980. Mechanics of discontinuous faults. J. Geophys. Res. Solid Earth 85, 4337–4350.
Shipton, Z.K., Evans, J.P., Kirschner, D., Kolesar, P.T., Williams, A.P., Heath, J., 2004. Analysis of CO2 leakage through 'low-permeability'faults from natural reservoirs in the Colorado Plateau, east-central Utah. In: Baines, S.J., Worden, R.H. (Eds.), Geological Storage of Carbon Dioxide. Geological Society, London, pp. 43–58. Special Publications.
Sibson, R.H., 1996. Structural permeability of fluid-driven fault-fracture meshes. J. Struct. Geol. 18, 1031–1042.
Talwani, P., 1999. Fault geometry and earthquakes in continental interiors. Tectonophysics 305, 371–379.
Tamagawa, T., Pollard, D.D., 2008. Fracture permeability created by perturbed stress fields around active faults in a fractured basement reservoir. Am. Assoc. Petrol. Geol. Bull. 92, 743–764.
Tavarnelli, E., Pasqui, V., 2000. Fault growth by segment linkage in seismically active settings: examples from the Southern Apennines, Italy, and the Coast Ranges, California. J. Geodyn. 29, 501–516.
Verhaert, G., Muchez, P., Keppens, E., Sintubin, M., 2009. Fluid impact and spatial and temporal evolution of normal faulting in limestones. A case study in the Burdur-Isparta Region (SW Turkey). Geol. Belg. 12, 59–73.
Virk, H., Singh, B., 1993. Radon anomalies in soil-gas and groundwater as earthquake precursor phenomena. Tectonophysics 227, 215–224.
Walsh, J., Bailey, W., Childs, C., Nicol, A., Bonson, C., 2003. Formation of segmented normal faults: a 3-D perspective. J. Struct. Geol. 25, 1251–1262.
Yoshida, H., Metcalfe, R., Yamamoto, K., Murakami, Y., Hoshii, D., Kanekiyo, A., Naganuma, T., Hayashi, T., 2008. Redox front formation in an uplifting sedimentary rock sequence: an analogue for redox-controlling processes in the geosphere around deep geological repositories for radioactive waste. Appl. Geochem. 23, 2364–2381.